MATERIALS SCIENCE

Regulating the absorption spectrum of polydopamine

Yuan Zou[1], Xiaofeng Chen[1], Peng Yang[1], Guijie Liang[2], Ye Yang[3], Zhipeng Gu[1], Yiwen Li[1]*

Polydopamine (PDA) has been increasingly exploited as an advanced functional material, and its emergent light absorption property plays a crucial role in determining various utilizations. However, the rational design and efficient regulation of PDA absorption property remain a challenge due to the complex structure within PDA. In this work, we propose a facile method to regulate the light absorption behaviors of PDA by constructing donor-acceptor pairs within the microstructures through the chemical connections between indoledihydroxy/indolequinone and their oligomers with 2,2,6,6-tetramethylpiperidine-1-oxyl moiety. The detailed structural and spectral analysis, as well as the density functional theory simulation, further confirms the existence of donor-acceptor molecular pair structures, which could decrease the energy bandgap and increase the electron delocalization for enhancing light absorption across a broad spectrum. These rationally designed PDA nanoparticles with tunable absorption properties also show improved total photothermal effect and demonstrate excellent performances in solar desalination.

INTRODUCTION

Melanin describes a class of biomacromolecular pigments widely distributed in nature, which has gradually become the focus of interest due to their outstanding properties, including anti–ultraviolet (UV) (*1*), metal chelating (*2*), free radical scavenging (*3*), and thermoregulation (*4*, *5*). Inspired by nature melanin and mussel adhesive proteins, polydopamine (PDA) has received increasing attentions in the past years for surface modifications, photothermal therapy, and bioimaging (*6*–*9*). In addition, the strong adhesive and light absorption properties of PDA are beneficial for interface engineering in water remediation (*10*, *11*). Many synthetic methods including electrochemical polymerization, self-oxidation polymerization, and enzymatic polymerization have been reported to prepare PDA nanomaterial with a decay absorption across the range of 200 to 1400 nm (*12*, *13*). However, only very limited attentions have been paid to regulate its absorption spectrum because of the structural heterogeneity and disorder covalent/noncovalent interactions of PDA. The dopamine polymerization process involves several complicated pathways, including catechol oxidation, rearrangement, chemically cross-linking, physically π-π stacking, and cation-π interaction, which have not been fully understood (*8*, *14*–*16*). Up to now, it has only reached a general conclusion that the main structural units within the PDA system include noncyclized dopamine units, 5,6-dihydroxyindole (DHI), indole-5,6-quinone (IQ), and their oligomers (*4*, *17*). The IQ unit can provide sufficient conjugated structures within PDA for a wide range of absorption (*4*). The chemical connections between DHI and IQ unit can also be regarded as electron donor and acceptor pairs to influent the energy bandgap and the light absorption property of PDA system (*18*, *19*). Therefore, we speculate that the construction of highly conjugated structures and donor-acceptor pairs within the PDA microstructures might be the key to regulate the absorption spectrum of PDA.

The development of donor-acceptor pair structures has been successfully used in the fields of organic polymer solar cells and organic field-effect transistors, resulting in a designed material with a broader absorption and higher carriers' mobility (*20*, *21*). In the PDA system, the introduction of additional moieties into structural units for generating a large variety of donor-acceptor pairs can also be a straightforward way to decrease the inherent energy bandgap and promote the electron transfer, lastly achieving the light absorption regulation of these bioinspired polymers. Notably, although several kinds of PDA-based photothermal materials have been well documented, their light energy harvesting efficiencies are not that high in both aqueous and solid states (*22*). Therefore, it is still interesting and desirable to further promote the light absorption capabilities and photothermal behaviors of PDA-based nanomaterials via rationally structural and functional tailoring. 2,2,6,6-Tetramethylpiperidine-1-oxyl (TEMPO) is a typical stale nitroxyl radical and well known for its applications in radical polymerization and organic oxidation reactions. It can oxidize phenol group into quinone group rapidly and then induce dopamine to polymerize (*23*, *24*), which can form several donor-acceptor pair structures with DHI, IQ moieties, and their oligomers by covalent coupling. So, our light absorption tuning strategy of PDA can be simply achieved by the copolymerization of TEMPO and dopamine.

In this work, we have developed a one-pot strategy to fabricate PDA nanoparticles (NPs) with tunable light absorption properties via the direct copolymerization of TEMPO and dopamine in an aqueous solution. The doping of TEMPO moiety into the PDA microstructures by covalently connecting with DHI/IQ oligomers can narrow the energy bandgap and improve the light absorption behavior of conventional PDA NPs (Fig. 1A), which is further confirmed by the electrochemistry analysis, density functional theory (DFT) simulation, and spectral measurements. The resulting TEMPO-doped PDA NPs with enhanced light absorptions across a broad spectrum also demonstrate outstanding photothermal efficiencies, which can be further used in the interfacial solar steam generation and seawater desalination.

[1]College of Polymer Science and Engineering, State Key Laboratory of Polymer Materials Engineering, Sichuan University, Chengdu 610065, China. [2]Hubei Key Laboratory of Low Dimensional Optoelectronic Materials and Devices, Hubei University of Arts and Science, Xiangyang 441053, China. [3]State Key Laboratory of Physical Chemistry of Solid Surfaces, College of Chemistry and Chemical Engineering, Xiamen University, Xiamen 361005, China.
*Corresponding author. Email: ywli@scu.edu.cn

RESULTS

Synthesis and characterization of TEMPO-doped PDA

The newly designed PDA NPs were facilely obtained through a one-pot polymerization of TEMPO and dopamine in an aqueous solution at room temperature (Fig. 1B). Three kinds of PDA NPs [named PDA-*i*

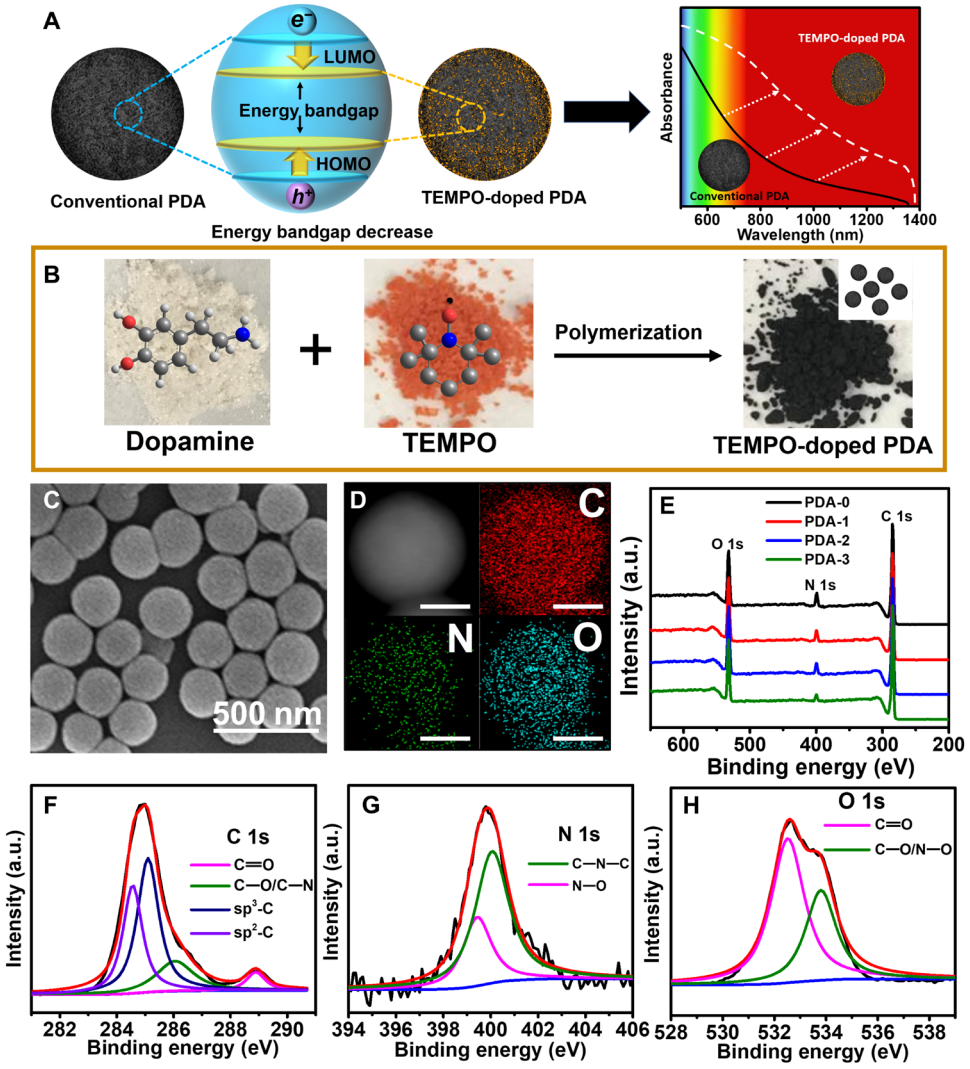

Fig. 1. Synthesis and characterization of TEMPO-doped PDA. (**A**) Schematic illustration of the TEMPO-doped PDA with narrower bandgap and improved light absorption ability compared to conventional PDA. (**B**) Polymerization of dopamine and TEMPO, together with their molecular structures and powder photographs. (**C**) SEM image of PDA-3. (**D**) EELS mapping analysis of PDA-3 (Scale bars, 100 nm). (**E**) XPS survey spectra of PDA-*i* (*i* = 0 to 3). a.u., arbitrary units. (**F**) C 1s peaks, (**G**) N 1s peaks, and (**H**) O 1s peaks in XPS spectra of PDA-3.

(*i* = 1 to 3)] with different doping contents and similar particle sizes were prepared by tuning the initial concentrations of TEMPO. Conventional PDA NP (PDA-0) was also synthesized by the self-polymerization of dopamine in the presence of ammonium by following the well-established method (*25*). Scanning electron microscopy (SEM) images and dynamic light scattering (DLS) results showed that all PDA-*i* (*i* = 0 to 3) samples with uniform size around ~230 nm were successfully prepared to eliminate the particle size effects (Fig. 1C and fig. S1, A to D). Zeta potential values of PDA-*i* (*i* = 0 to 3) were measured as −35.3, −26.0, −28.3, and − 28.8 mV, respectively, suggesting their good dispersion and stability of in water. Note that a new characteristic peak at 1352 cm^{-1} was observed in Fourier transform infrared (FTIR) spectra of all PDA-*i* (*i* = 1 to 3) samples compared to the spectrum of PDA-0, which was attributed to N—O stretching vibrations from TEMPO moieties (fig. S1E) (*24*). In addition, the electron energy-loss spectroscopy (EELS) elemental mapping images of PDA-3 showed that the C, N, and O elements were uniformly distributed within the spherical-shaped PDA NPs (Fig. 1D). X-ray photoelectron spectroscopy (XPS) characterization was also carried out to confirm the existence of C, N, and O elements in the survey spectra of all PDA samples (Fig. 1E). For example, the 1s peak of carbon (C 1s) of PDA-3 mainly consisted of four types of carbon bonds (*24*, *25*): sp^2-C (C═C) peak at 284.5 eV, sp^3-C (C—C) peak at 285.1 eV, C—OH (hydroxyl) and C—N at 286.1 eV, and C═O at 288.9 eV, respectively (Fig. 1F). Moreover, N—O at 399.4 eV and C—N—C (pyrrolic nitrogen) at 400.1 eV were also observed in the peak of N 1s, also demonstrating the existence of pyrrolic rings and TEMPO moieties in PDA-3 (Fig. 1G) (*26*). Notably, the N 1s peaks of PDA-*i* (*i* = 0 to 3) were differentiated and used to estimate the amount of C—N—C and N—O bonds within PDA structures, which indicated the doping content of TEMPO within PDA-*i* (*i* = 1 to 3) were approximately 11, 19, and 23%, respectively (fig. S1, F to I). In the O 1s region, the two peaks represented C═O bond at 532.5 eV and C—O/N—O bond at 533.8 eV, which were

consistent with the single- and double-bonded oxygen functionalities of the O 1s core level peak (Fig. 1H and fig. S1, J to M) (*27*). All the characterizations above clearly demonstrated that we had successfully prepared the TEMPO-doped PDA NPs.

We then discussed the possible copolymerization mechanism and detailed macromolecular structures of PDA. As proposed in fig. S2A, we hypothesized that the formation of TEMPO-doped PDA might follow two pathways. In path 1, dopamine molecule was first oxidized by TEMPO radical (*23*, *24*), subsequently resulting in the dopamine quinone and DHI intermediate after the oxidation and rearrangement process (*28*). This hypothesis was evidenced by the observation of the pyrrolic nitrogen in N 1s peak of XPS (Fig. 1G). In path 2, TEMPO first attached onto the benzene ring to form a dopamine-TEMPO conjugate, which could rearrange into DHI-TEMPO consequentially (*24*). In addition, the DHI-TEMPO might further transform into $(DHI)_2$-TEMPO and $(IQ)_2$-TEMPO intermediates continuously. Note that the corresponding mass/charge ratio peaks of most proposed intermediate molecules could be observed in the electrospray ionization mass spectrometry (ESI-MS) spectrum of the crude product solution after 5-min reaction (fig. S2, B and C). Last, the copolymerization of those intermediates such as DHI, $(DHI)_2$-TEMPO, and $(IQ)_2$-TEMPO could further achieve the TEMPO-doped PDA with cross-linking macromolecular structure.

Enhanced light absorption and photothermal behavior of TEMPO-doped PDA

We next carefully examined the light absorption ability and total photothermal effect of these prepared TEMPO-doped PDA NPs. Figure 2A showed the photographs of PDA-*i* (i = 0 to 3) aqueous solutions with different concentrations (50 and 100 μg ml^{-1}). The blackness of PDA-0 was far less than those of the other three TEMPO-doped PDA samples at the same concentration, which suggested that TEMPO-doped PDA NPs had stronger absorption ability than conventional PDA-0 across the visible light range by naked-eye observation. To quantitatively analyze the chromatic aberration of the PDA solutions, we measured Commission Internationale de l'Eclairage colors variables in Fig. 2B and fig. S3 (A and B). The histograms showed that the three main color values (L^*, a^*, and b^*) of PDA-0 were higher than those of PDA-*i* (i = 1 to 3), which indicated that the TEMPO-doped PDA NPs were able to absorb more visible lights for exhibiting higher blackness. Notably, for PDA-*i* (i = 1 to 3), L^*, a^*, and b^* values were also gradually decreasing with the increase in TEMPO concentration within PDA NPs. In addition, in the UV-visible–near-infrared (UV-vis-NIR) absorbance spectra of PDA samples, PDA-*i* (i = 1 to 3) showed much stronger absorptions at both of visible and NIR regions compared to PDA-0 (Fig. 2C). Higher TEMPO doping concentration also resulted in the stronger light adsorption performance in PDA-*i* (i = 1 to 3). As the concentration of PDA-3 gradually increasing from 12.5 to 200 μg ml^{-1}, the light adsorption value of PDA-3 also increased in a linear relationship, coupled with a color change of the aqueous solution from colorless to dark (fig. S3, C to F). The strong light absorption ability of TEMPO-doped PDA NPs could allow catching and converting solar energy to heat efficiently for a wide range of applications.

To further evaluate the photothermal effect of TEMPO-doped PDA, we dispersed PDA-3 in water at several concentrations ranging from 25 to 100 μg ml^{-1} and then irradiated it by 635- and 808-nm laser, respectively, for 600 s (Fig. 2D and fig. S3G). With the increase in NP concentration, the temperatures increased quickly reaching as high as 58.1°C (635-nm laser irradiation) and 71.3°C (808-nm laser irradiation), respectively. In contrast, the temperature of pure water was only increased by 7.8°C (635-nm laser irradiation) and 2.6°C (808-nm laser irradiation) in 10 min. Next, we found that the temperature elevations of PDA NPs gradually increased as the increase in the doping TEMPO content. Notably, the increasing temperatures (ΔT) of PDA-3 could be 35.3° and 47.8°C upon 10-min irradiation by 635- and 808-nm light, respectively, while the ΔT of PDA-0 increased by only 28°C (635 nm) and 23.4°C (808 nm) under the same condition (Fig. 2E and fig. S3H). After four on/off cycles under 635- and 808-nm light irradiation, the temperature elevation behavior of PDA-3 remained quite stable, which was beneficial for the practical usage (Fig. 2F and fig. S3I). We then calculated the total photothermal conversion efficiency (η*) of the PDA NPs according to Eq. 1

$$\eta = \frac{hA\Delta T_{max} - Q_S}{I} \quad (1)$$

where h is the heat transfer coefficient, A is the surface area of the container, ΔT_{max} is the temperature change of the PDA solution between the maximum system temperature and the ambient surrounding temperature, I is the laser power, Q_S is the heat associated with the light absorbance of the solvent, and η* is the total photothermal conversion efficiency. The lumped quantity hA was determined by measuring the rate of temperature drop after the laser was shut off. The value of hA was derived from Eq. 2

$$\tau_s = \frac{m_D c_D}{hA} \quad (2)$$

where τ_s is the sample system time constant [linear time data versus $-\ln\theta$ obtained from the cooling period shown in fig. S3 (K to S)] and m_D and c_D are the mass and heat capacity of deionized water used as the solvent, respectively. According to Eqs. 1 and 2, the η^*_{635} values of PDA-*i* (i = 0 to 3) were calculated as 16.7, 22.2, 26.0, and 29.1%, respectively. In addition, the η^*_{808} values were calculated as 13.1, 18.6, 21.0, and 25.6%, respectively. To further evaluate the light absorption capability of PDA-*i* (i = 0 to 3), we both calculated their molar extinction coefficient at 635 nm (visible light) and 808 nm (NIR light). The ε_{635} values of the PDA-*i* (i = 0 to 3) were calculated to be 3.0×10^9, 3.9×10^9, 5.1×10^9, and 5.7×10^9 M^{-1} cm^{-1}, respectively, while the ε_{808} values of the PDA-*i* (i = 0 to 3) were calculated to be 1.2×10^9, 2.7×10^9, 3.8×10^9, and 4.5×10^9 M^{-1} cm^{-1}, respectively, both suggesting the enhanced light absorption capabilities of TEMPO-doped PDA NPs (Fig. 2G). Notably, even compared with many outstanding photothermal materials, the TEMPO-doped PDA NPs also showed higher molar extinction coefficient values (*29*, *30*). Note that these PDA NPs with tunable light absorption could even exhibit better photothermal behaviors than many well-established photothermal materials, including Au NP and carbon black. Under the same conditions, it was found that the ΔT of Au NPs was only 12.1°C (635-nm laser irradiation) and 10.1°C (808-nm laser irradiation), respectively, which were much lower than those of the TEMPO-doped PDAs (fig. S4, A to D). In addition, the total photothermal efficiencies were measured as only 9.3% under 635-nm laser irradiation and 7.9% under 808-nm laser irradiation. In addition, the Au NPs might suffer substantial loss of the light absorbance after long-term irradiation due to the destruction of the structure (melting) during

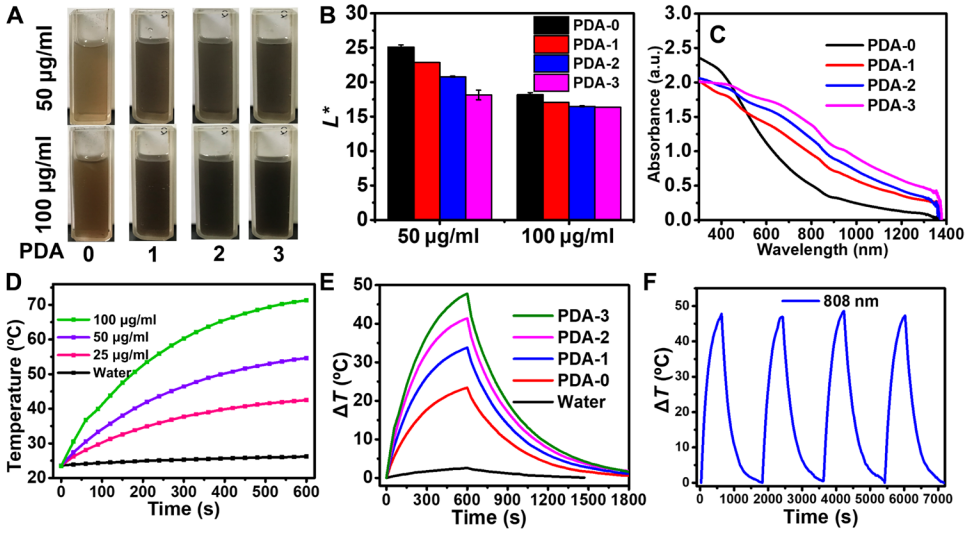

G Sample		PDA-0	PDA-1	PDA-2	PDA-3
Molar extinction coefficient (M^{-1} cm^{-1})	ε_{635}	3.0×10^9	3.9×10^9	5.1×10^9	7×10^9
	ε_{808}	1.2×10^9	2.7×10^9	3.8×10^9	4.5×10^9
ΔT_{635} (°C)		28.0	33.8	41.4	35.3
ΔT_{808} (°C)		23.4	29.8	31.3	47.8
Total photothermal efficiency (%)	η^*_{635}	16.7	22.2	26.0	29.1
	η^*_{808}	13.1	18.6	21.0	25.6

Fig. 2. Enhanced light absorption and photothermal behavior of TEMPO-doped PDA. (**A**) Photographs of PDA aqueous solutions with concentration of 50 and 100 μg ml^{-1}. Photo credit: Yuan Zou, Sichuan University. (**B**) *L** values of different PDA aqueous solutions. (**C**) UV-vis-NIR spectra of PDA-*i* (*i* = 0 to 3) ranging from 300 to 1500 nm. (**D**) Temperature elevations of PDA-3 at different concentrations under 808-nm laser irradiation. (**E**) The photothermal response of PDA-*i* (*i* = 0 to 3) aqueous solutions (100 μg ml^{-1}) for 600 s with 808-nm laser irradiation, and then the laser was shut off. (**F**) Temperature curves of PDA-3 (100 μg ml^{-1}) under four on/off cycles and under 808-nm laser irradiation. The light intensity of 808-nm laser was 2.0 W cm^{-2}. (**G**) Molar extinction coefficient, Δ*T*, and total photothermal efficiency of PDA-*i* (*i* = 0 to 3). Photo credit: Yuan Zou, Sichuan University.

the heating process (fig. S4, E to G). For carbon black, the Δ*T* values were measured as 25.5°C (635-nm laser irradiation) and 44.9°C (808-nm laser irradiation), and the total photothermal efficiency values were calculated to be 22.5 and 23.2%, respectively, which were all lower than those of PDA-3 under the same test conditions (fig. S4, H to K). Therefore, we could conclude that those TEMPO-doped PDA NPs clearly demonstrated enhanced light absorption ability and improved photothermal behaviors compared to conventional PDA-0 and many other kinds of photothermal nanomaterials, which could serve as the new generation of photothermal agents with various utilizations.

Structural analysis and absorption property regulation of TEMPO-doped PDA

We then carefully discussed the mechanism of enhanced light absorption ability and photothermal effect of PDA by doping of TEMPO unit via the detailed structural analysis. In general, to improve the light absorption ability of polymeric materials, mainly replied on the decrease in energy bandgap and the increase in electron delocalization, which could be achieved by the construction of donor-acceptor pair structures. In TEMPO-doped PDA system, the spontaneous formation of donor-acceptor microstructures based on the chemical conjugates between TEMPO and DHI, IQ, and their oligomers was established during the polymerization process, which could contribute to lower the energy bandgap and result in the enhancement of light absorption (*31*–*33*). To verify this point, we calculated the optical bandgap (E_g^{opt}) value of PDA-0 to be ~0.96 eV, and those of PDA-*i* (*i* = 1 to 3) were all around ~0.81 eV from the absorption edge of their aqueous solutions in Fig. 2C. Then, we carried out electrochemical cyclic voltammetry (CV) to investigate the electronic energy bandgaps (E_g) for all the samples (Fig. 3A). The highest occupied molecular orbital (HOMO) and the lowest unoccupied molecular orbital (LUMO) energy levels of the PDAs were measured by CV measurements, with Ag/AgCl as a reference electrode and Fc/Fc^+ couple as an internal reference. The HOMO/LUMO energy levels (E_{HOMO}/E_{LUMO}) were estimated from the onset oxidation potential (E_{ox}) and onset reduction potential (E_{red}) according to the equation of $E_{LUMO/HOMO} = -e\,(E_{ox}/E_{red} + 4.44)$ (in electron volts) (*34*). (In our electrochemical workstation system, $E_{Fc/Fc+}$ was measured to be 0.36 versus Ag/AgCl in fig. S5A.) From the CV curves of PDAs shown in Fig. 3A, the E_{ox}/E_{red} of PDAs were measured as 0.38 V/−0.52 V, 0.43 V/−0.36 V, 0.41 V/−0.37 V, and 0.43 V/−0.37 V, respectively. According to the equation mentioned above, the E_{HOMO}/E_{LUMO} of PDAs were calculated to be −4.72 eV/−3.92 eV, −4.87 eV/−4.08 eV, −4.85 eV/−4.07 eV, and − 4.87 eV/−4.07 eV, respectively. Related energy levels were summarized in Fig. 3B. In comparison with PDA-0, the E_{LOMO} of PDA-*i* (*i* = 1 to 3) all decreased with the increase in the doped TEMPO unit (E_{HOMO}/E_{LUMO} = −5.02 eV/−2.94 eV, calculated from fig. S5B). It was revealed that TEMPO unit could be regarded as a donor fragment due to the transition of electron from the HOMO of donor to the LUMO of acceptor. Compared with PDA-0, the E_g of PDA- i (*i* = 1 to 3)

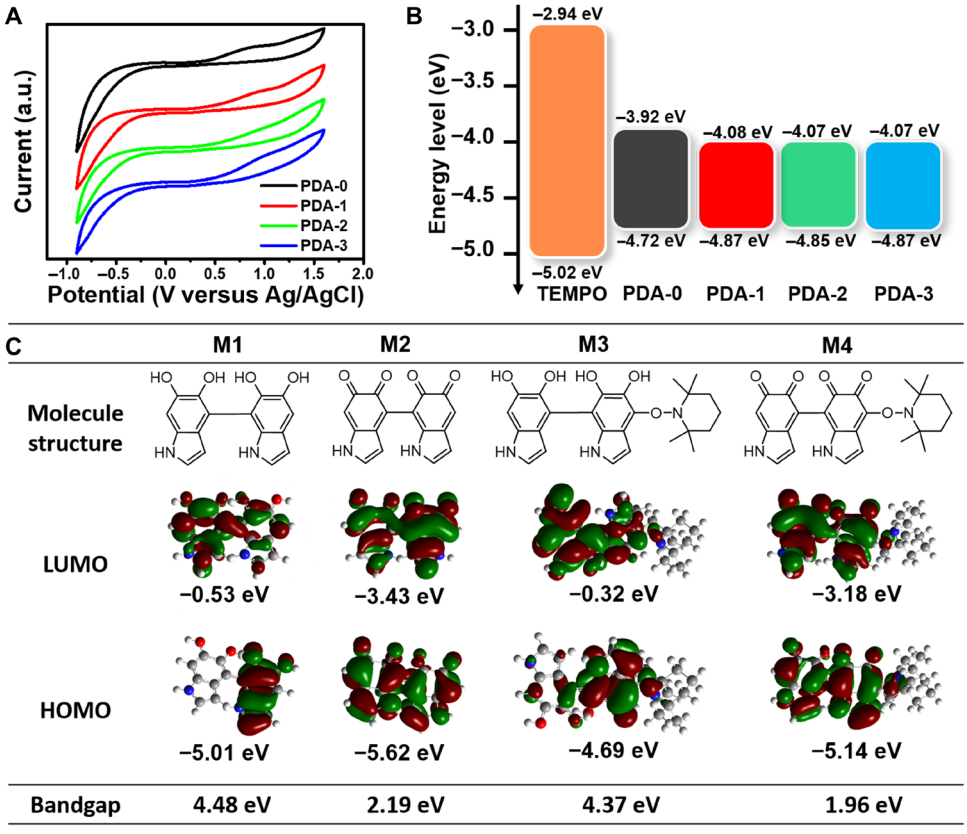

Fig. 3. Electrochemical and DFT measurement of PDA-*i* (*i* = 0 to 3). (**A**) CVs of PDA-*i* (*i* = 0 to 3). (**B**) Schematic illustration of the energy levels of TEMPO and PDA-*i* (*i* = 0 to 3). (**C**) Chemical structures of possible moieties within PDA microstructure and theoretical calculated frontier molecular orbital using DFT calculations at the B3LYP/6-31 G(d, p) level.

became narrowed, which could contribute to a better light absorption capability. In addition, we also carried out the theoretical calculations of possible donor-acceptor molecular conjugated structures within the PDA system by DFT method at the B3LYP/6-31 G(d, p) level for understanding the relationship between the structure and function of PDA. We hypothesized that PDA consisted of three main moieties, which were DHI, IQ, and TEMPO. As shown in Fig. 3C, four possible typical molecular pairs of PDAs were presented as M1, M2, M3, and M4. The LUMO/HOMO energy levels of M1, M2, M3, and M4 were calculated to be −0.53 eV/−5.01 eV, −3.43 eV/−5.62 eV, −0.32 eV/−4.69 eV, and − 3.18 eV/−5.14 eV, and their bandgaps were 4.48, 2.19, 4.37, and 1.96 eV, respectively. According to the electron cloud distribution, M2 had higher density of delocalized π electrons, which was able to extend the conjugated structure and enhance planarity of the moiety resulting in lower bandgap than that of M1 (*35*). From M3 and M4, it was found that the addition of TEMPO moiety could further improve the electron delocalization and decrease the bandgap. Note that the main conjugation point of the connected indole units might also be position 2, we also further carried out a series of calculations of LUMO/HOMO energy levels of other possible moieties within the PDA system, which again showed the similar results (fig. S6, A to C). Furthermore, the O 1s peaks of PDA-*i* (*i* = 0 to 3) were differentiated and imitated to estimate the amount of C—O and C═O bonds within PDA structures (fig. S1, J to M). As the doping concentration of TEMPO increasing, the proportion of IQ moiety also gradually increased, which could lastly result in the better delocalization of electrons and light absorption ability.

As discussed above, the TEMPO-doped PDAs with enhanced light absorptions across the visible and NIR regions were able to catch more solar energy under irradiation compared with conventional PDA. To exhibit the excellent photothermal performance, the nonthermal radiative transition process should also be minimized to enhance the photoconversion behavior of this system. Fortunately, the doping of TEMPO radical might be a favor to directly increase the free radical concentration within PDA, which could help to restrict the nonthermal radiative transition processes. Electron paramagnetic resonance (EPR) measurement was carried out to verify this hypothesis. PDA-*i* (*i* = 1 to 3) displayed much higher EPR signal intensities than PDA-0 at the same mass in the solid state (Fig. 4A), which confirmed the increase in free radicals within PDA by doping of TEMPO. Notably, EPR signals of both radicals from PDA (~3512 G) and TEMPO (~3480 G) were both observed but overlapped. To further understand the light energy conversion process in PDA, we measured the exciton dynamics in PDA by transient absorption spectroscopy. After optical excitation, excitons created in these polymers could induce a transient absorption in NIR region (Fig. 4B). As spectral shape of the exciton-induced absorption (EIA) did not depend on the doping amount of TEMPO, we could tentatively attribute the EIA to the presence of excitons in the polymerized DHI and IQ. The spectral magnitude of EIA decayed rapidly as the pump-probe delay increasing, while the spectral shape did not evolve during the decay (Fig. 4C). Moreover, the EIA kinetic traces of all samples showed a decay with an identical trend, offering the further evidence that excitons were exclusively residing in the polymers. These kinetic

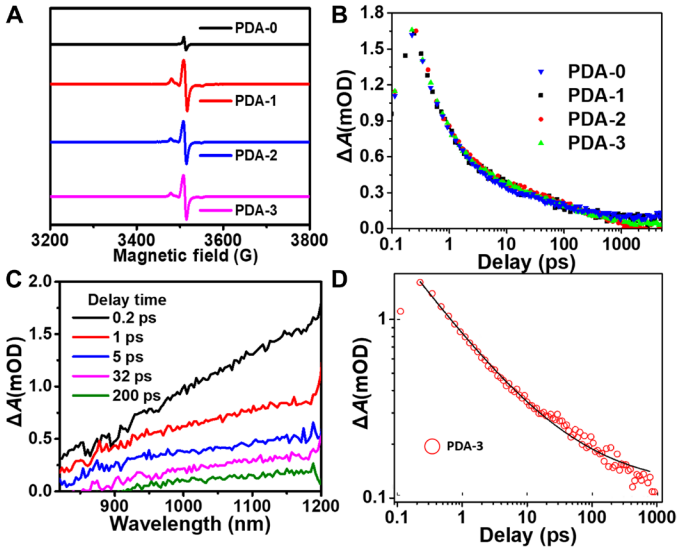

Fig. 4. The light energy conversion process within PDA. (**A**) EPR spectra of PDA-*i* (*i* = 0 to 3) with the same mass in the solid states. (**B**) Transient absorption kinetics traces for PDA-*i* (*i* = 0 to 3). (**C**) Transient absorption spectra of PDA-3 at indicated delay times. (**D**) The EIA kinetic trace of PDA-3. mOD, mean optical density.

traces decayed to negligible small by 1 ns, and the decay could be described by a power law function with a power of −0.50 ± 0.01 (Fig. 4D and fig. S7, A to C). The power law kinetics was indicative of a broad distribution of exciton recombination rate, implying that the excitons might be not restricted to a DHI or IQ units, and they might diffuse to the adjacent units located in a highly disordered structure (*36*). Considering that the photoluminescence of these polymers was too weak to be detected (equipment model), the fast exciton decay must be dominated by the nonradiative recombination (fig. S7, D to I). Thus, exciton recombination in PDA could only occur via emitting phonons to satisfy the energy conservation. That is, the absorbed photon energy stored in excitons quickly transferred into the molecular vibrations, i.e., increasing temperature of the polymers. The exciton recombination was completed within 1 ns, suggesting that, after photon absorption, the thermal energy accumulation should also be on this time scale. Considering the low thermal diffusivity in polymers, thermal energy dissipation must be much slower than the accumulation, which rationalized the high photothermal conversion efficiency. Above all, we could clarify that the total photothermal effect of the TEMPO-induced PDA could be improved by enhancing the light absorption ability via the covalently linking of donor-acceptor fragments within PDA. In addition, we found that there was hardly the nonthermal radiative transition process within the PDA system.

Water desalination application

The excellent light absorption and photothermal property of TEMPO-doped PDA offered unique opportunities in water steam generation and seawater desalination. PDA-3 with the best photothermal effect was chosen as the promising candidate for the further fabrication of evaporation device. First, PDA-3 aqueous solution (10 mg ml^{-1}, 2 ml) was deposited onto a cellulose membrane (CM) to form a double-layer structured membrane as a hydrophilic light absorber. To decrease the thermal loss and make the light absorber float on the water surface, we selected a polystyrene (PS) foam (thickness, ~2.24 cm) as a thermal insulation layer to prevent the device from contacting with the bulk water directly. A cotton swab (diameter, ~0.7 cm) was inserted into the center of the PS foam for water transportation through capillary effect, and then the evaporator device was floated on the water surface (Fig. 5A). When irradiated with solar light, purified water was obtained by collecting the condensed water from the solar steam. The photographs of blank CM and PDA-coated CM were shown in Fig. 5B. As shown in Fig. 5C, PDA-3 successfully adhered to the CM, and they could be rinsed by water for many times without peeling. As shown in fig. S8A, the PDA-3–coated CM showed improved light absorption ability compared to PDA-0–coated CM and blank CM sample. It was found that the absorbance of PDA-3–coated CM was ~94 and 88% in the UV (200 to 400 nm) and visible (400 to 780 nm) regions, respectively. Therefore, the PDA-3–based device could absorb majority of solar energy across the main spectrum. Under one-sun illumination, the surface temperature of PDA-3–coated CM rose rapidly to ~37°C within 1 min (fig. S8B), and the central temperature was steady at ~39.5°C eventually (Fig. 5E). With the PS foam insulator, the absorbed solar energy was highly located on the PDA-3–coated CM. Notably, the temperature of PS foam was approximately kept at the room temperature under illumination, which showed that the heat loss to the bulk water was successfully suppressed.

To further investigate the performance of solar vapor generation of PDA-3–coated CM, we measured the weight loss of water during evaporation. As shown in Fig. 5F, the evaporation rates of saline water [3.5 weight % (wt %) NaCl], CM, and PDA–coated CM were measured as 0.456, 0.672, and 1.534 kg m^{-2} $hour^{-1}$, respectively. Under the dark condition, the evaporation rate of the device was only 0.168 kg m^{-2} $hour^{-1}$. To determine the photothermal evaporation performance of our device, we considered the energy conversion efficiency as an important index, which was defined as $\eta_{ep} = mh_{LV}/I$, where m is the mass flux (evaporation rates under one-sun illumination − evaporates in the dark), h_{LV} is the total enthalpy of liquid-vapor phase change (sensible heat + phase change enthalpy), and I is the power density of solar illumination. In the experiment, the solar energy conversion efficiency of the PDA-coated CM could reach 88.6% under one-sun irradiation, which was much higher than the 28.6% of bulk water and 32.3% of the pure CM (Fig. 5G). When the power density of solar simulator increased to four suns, the PDA-3–coated CM could be quickly heated up, and visible steam flow was generated on the top of the membrane (movie S1). In addition, the photograph of visible steam flow on top of the water surface under illumination of a solar simulator at four suns was also shown in Fig. 5H. Furthermore, both of saline water and seawater from Bohai Bay were used to examine the desalination effect of our device, and the concentration of metal ions was measured by inductively coupled plasma optical emission spectrometer (ICP-OES). For the saline water, the concentration of Na^+ was sharply decreased by at least four orders of magnitude in the condensation chamber after desalination, which was substantially below the salinity levels defined by the World Health Organization (WHO) and the U.S. Environmental Protection Agency (EPA). The concentrations of four main ions in Bohai seawater (Na^+, Mg^{2+}, Ca^{2+}, and K^+) were also tested. The extremely low ion concentrations after desalination ensured that the performance of our device for desalination was feasible (Fig. 5I). Note that the salt deposited on the CM surface during the evaporation could be also easily washed away by saline water. The durability of the PDA-3–coated CM was also investigated by 30 cycles

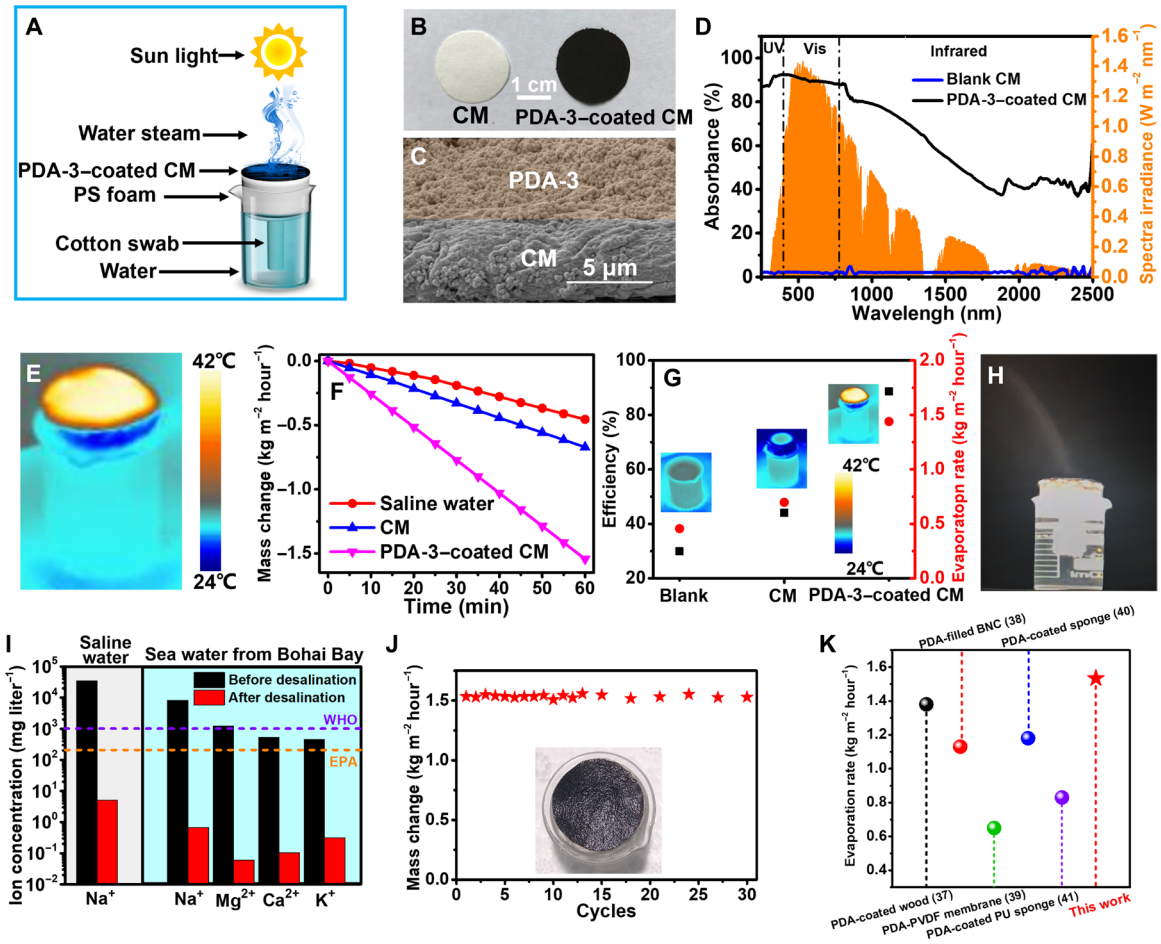

Fig. 5. Water desalination experiment. (**A**) A schematic diagram of the solar steam evaporation device based on PDA-3. (**B**) Photograph of the CM and PDA-3–coated CM. (**C**) SEM cross-section image of the double-layered film structure. (**D**) UV-vis-NIR diffuse reflection spectra of the CM and PDA-3–coated CM in the wavelength range of 250 to 2500 nm. (**E**) IR image of PDA-3–based device under one sun for 15 min. (**F**) Time course of water evaporation performances of saline water, CM, and PDA-3–coated CM under one sun irradiation. (**G**) Solar steam efficiency and evaporation rate of saline water, CM, and PDA-3–coated CM. (**H**) Photograph of the water steam generated under solar illumination of four suns with the PDA-3–coated CM. (**I**) The ion concentration of the saline water and seawater obtained from Bohai Bay before and after desalination. The dashed lines refer to the standard for drinkable water from the World Health Organization (WHO) and U.S. Environmental Protection Agency (EPA), respectively. (**J**) Evaporation cycle performance of solar desalination devices over 30 cycles, with each cycle sustained more than 1 hour. The inset showed the photograph of absorber after 30 cycles. (**K**) Evaporation rate among different PDA-based evaporators under one-sun illumination. PVDF, polyvinylidene difluoride. Photos credit: Yuan Zou, Sichuan University.

experiments (1 hour for each cycle), indicating excellent recycle stability (Fig. 5J). In addition, the morphology and structure of PDA on the surface remained unchanged after 30 cycles of water evaporation (Fig. 5J and fig. S8, C and D). Notably, the PDA-3–coated CM was found to exhibit a higher evaporation rate than many of the established PDA-based evaporators under one-sun illumination (Fig. 5K and table S2) (*37*–*41*). All the results demonstrated that the highly efficient and durable solar desalination device based on PDA-3 sample has been successfully fabricated.

DISCUSSION

In summary, we proposed a facile method to regulate the absorption spectrum of PDA via a one-pot polymerization of dopamine and TEMPO. In addition, the resulting NPs exhibited improved light absorption ability and total photothermal effect compared to conventional PDA nanomaterials, which was rationally achieved by constructing of donor-acceptor structures within the PDA system to decrease the energy bandgap and increase the electron delocalization. Besides, it was found that the doping of TEMPO would not influence the main polymer structure and photothermal mechanism and the nonthermal radiation was hardly found in PDA systems. The resulting TEMPO-doped PDA was coated on the CM film as the sunlight absorber to fabricate a water evaporation device, which could exhibit excellent evaporation rate of ~1.53 kg m^{-2} $hour^{-1}$ under one-sun irradiation with a high solar conversion efficiency (~88.6%). We believe that this work could offer opportunities toward the structural and functional tailoring of PDA nanomaterials for a wide range of light harvesting applications.

MATERIALS AND METHODS

Chemicals and materials

Dopamine hydrochloride (98%), TEMPO (99%), ammonia aqueous solution (25 to 28 wt %), NaCl (99%), acetonitrile (99.9%), tetrabutylammonium hexafluorophosphate (Bu_4NPF_6) (99%), and

ferrocene (99.5%) were all purchased from J&K Scientific Ltd. (Beijing, China). The cellulose film was obtained from Fushun city civil affairs filter paper factory. All chemicals were freshly used without further purification. Deionized water was used in all experiments.

Synthesis of PDA-0

The approach to synthesizing PDA-0 was according to a well-established method (*25*). Dopamine hydrochloride (500 mg, 2.64 mmol) was dissolved in a mixture of 90 ml of deionized water and 40 ml of ethanol under magnetic stirring for 10 min at room temperature. Ammonia aqueous solution (NH_4OH; 2.5 ml, 28 to 30%) was then injected into the above solution. The color of the solution immediately turned pale brown and gradually changed to black. After a 16-hour reaction, the PDA-0 sample was obtained by centrifugation and washed three times with deionized water.

Synthesis of PDA-*i* (*i* = 1 to 3)

As shown in table S1, different amounts of TEMPO (200 mg, 1.28 mmol; 300 mg, 1.92 mmol; and 400 mg, 2.56 mmol) were fully dissolved in 80 ml of deionized water under magnetic stirring for 20 min. Dopamine hydrochloride (200 mg) was dissolved in 20 ml of deionized water and then quickly injected into the above solutions. After stirring for 8 to 16 hours, the PDAs with the same sizes were obtained by centrifugation and washed three times with deionized water.

Characterization

The surface morphologies of the PDAs were acquired on SEM of FEI Quanta 250. The samples were prepared on the mica sheet (1 mm by 1 mm) by spin coater (KW-4A, Institute of Microelectronics, Chinese Academy of Science). The mica surface was freshly cleaved by lifting off a thin layer of mica sheet with an adhesive tape. A Hitachi HD-2300 dual energy-dispersive X-ray spectroscopy (EDS) cryo–scanning transmission electron microscopy was used for EDS mapping images. UV-vis-NIR transmission and reflection spectra were collected on a Shimadzu UV3600 UV-vis-NIR spectrometer. XPS measurements were conducted with a VG ESCALAB MKII spectrometer. The XPSPEAK software (version 4.1) was used to deconvolute the narrow-scan XPS spectra of the C 1s, O 1s, and N 1s of the samples, using adventitious carbon to calibrate the C 1s binding energy (284.5 eV). FTIR spectra were performed on a PerkinElmer Frontier FTIR spectrometer. DLS and zeta potential measurements were characterized by a Malvern Zetasizer Nano ZS particle analyzer, and all the samples were measured in aqueous solutions (pH 7). The ESI-MS spectrum of the crude reaction was measured by Applied Biosystems API 2000 using positive ion mode ESI. The crude product solution was injected into the spectrometer at a flow rate of 10 ml min^{-1} with the spray voltage of 5 kV and the pressure of sheath and auxiliary gas of 45 psi. CIELAB color variable values were measured on a 3nh colorimeter. EPR testing of NPs was performed on Bruker EPR EMX_Plus. The spectrometer was operated at X band (9.85 GHz), and the spectra were obtained with a 100-kHz field modulation at 0.1-mW power. The fluorescence and phosphorescence spectra were recorded on a fluorescence spectrophotometer (Model, F98). CV measurements were conducted on a CHI760E electrochemical workstation using sample film–coated indium tin oxide as the working electrode, Pt wire as the counter electrode, and Ag/AgCl as the reference electrode in a 0.1 M Bu_4NPF_6 acetonitrile solution. The Fc/Fc^+ couple was used as an internal reference. The metal ion content of the water was determined by ICP-OES (IRIS Advantage). All IR photographs were taken by an IR camera (FLIR, T540). The mass densities of PDA-*i* (*i* = 0 to 3) were determined by a gas displacement pycnometry system (AccuPyc 1340, Micromeritics).

The transient absorption measurement was based on the Ti:sapphire amplifier (Coherent Astrella, 800 nm, pulse duration of ~100 fs, ~6 mJ per pulse, and 1-KHz repetition rate) and the pump-probe transient absorption spectrometer (HELIOS Fire, Ultrafast Systems). Half of the output power of the amplifier was delivered to the pump-probe setup. The pump pulse (400 nm) was generated by doubling the frequency of the fundamental pulse (800 nm) based on a beta barium borate crystal, and its intensity was attenuated by two neutral density filter wheels. The broadband probe pulse (850 to 1400 nm) was generated by focusing the 800-nm fundamental pulse into a sapphire crystal. The pump-probe delay was controlled by an optical delay line stage, and the maximum time window is 5 ns. The pump and probe were focused and overlapped onto the polymer films on glass substrates.

Calculation of the molar extinction coefficient

$$\varepsilon = \frac{A V_{NPs} \rho N_A}{LC}$$

where ε is the extinction coefficient, A is the absorption at a certain wavelength of NPs, V_{NPs} is the average volume of the NPs, ρ is the density of NPs, N_A is Avogadro's constant, L is the path length, and C is the weight concentration of the NPs.

Photothermal performance measurements

To evaluate the photothermal effects of PDAs, Au NPs, and carbon black, 1-ml aqueous solution of each materials were introduced in a quartz cuvette and then irradiated with a 635-nm visible laser (1.8 W cm^{-2}) or an 808-nm NIR laser (2.0 W cm^{-2}) for 600 s, respectively. The cycles were repeated four times. A thermocouple probe (0.1°C accuracy) was inserted into the aqueous solutions perpendicular to the path of the laser. Another thermocouple probe (0.1°C accuracy) was inserted into pure water without irradiation as a negative control. The temperature was recorded by a digital thermometer with a thermocouple probe every 10 s.

Theoretical calculations

The energy levels of the molecular orbits were calculated through DFT by Gaussian 09 package (*42*). The molecular orbits of possible moieties were imported at the B3LYP/6-31 G(d, p) level.

Fabrication of PDA-3–based device

Ten milligrams of PDA-3 NP was dispersed in 5 ml of deionized water under the assistance of ultrasonic bath. The dispersed mixture was then deposited on the CM under vacuum. The composite film was placed on a heat plate, and the temperature was kept at 60°C for 30 min. After cooling, the film was stored in a petri dish for further use.

Steam generation and solar desalination experiments

The PDA-3–based film device (R = 1.3 cm) was placed on a punched PS foam (thermal conductivity ≈ 0.04 W $m{\cdot}K^{-1}$) with a cotton swab inserted in the center hole, and the entire structure was allowed to float on the surface of saline solution with the bottom side of the cotton swab in direct contact with bulk solution. The device was irradiated by a solar simulator (CEL-PE300L-3A), and the evaporation rate was measured for 60 min at steady-state condition. The

weight loss and the weight of collect clean water were measured by an electronic mass balance. The surface temperature of the device over the process was recorded by an IR camera.

SUPPLEMENTARY MATERIALS

Supplementary material for this article is available at http://advances.sciencemag.org/cgi/content/full/6/36/eabb4696/DC1

REFERENCES AND NOTES

1. S. Premi, S. Wallisch, C. M. Mano, A. B. Weiner, A. Bacchiocchi, K. Wakamatsu, E. J. H. Bechara, R. Halaban, T. Douki, D. E. Brash, Chemiexcitation of melanin derivatives induces DNA photoproducts long after UV exposure. *Science* **347**, 842–847 (2015).
2. Z. Wang, Y. Zou, Y. Li, Y. Cheng, Metal-containing polydopamine nanomaterials: Catalysis, energy, and theranostics. *Small* **16**, 1907042 (2020).
3. P. Yang, Z. Gu, F. Zhu, Y. Li, Structural and functional tailoring of synthetic melanin radical scavenger. *CCS Chem.* **2**, 128–138 (2020).
4. Y. Liu, K. Ai, L. Lu, Polydopamine and its derivative materials: Synthesis and promising applications in energy, environmental, and biomedical fields. *Chem. Rev.* **114**, 5057–5115 (2014).
5. M. d'Ischia, K. Wakamatsu, A. Napolitano, S. Briganti, J.-C. Garcia-Borron, D. Kovacs, P. Meredith, A. Pezzella, M. Picardo, T. Sarna, J. D. Simon, S. Ito, Melanins and melanogenesis: Methods, standards, protocols. *Pigment Cell Melanoma Res.* **26**, 616–633 (2013).
6. Y. Zou, Z. Wang, Z. Chen, Q.-P. Zhang, Q. Zhang, Y. Tian, S. Ren, Y. Li, Synthetic melanin hybrid patchy nanoparticle photocatalysts. *J. Phys. Chem. C* **123**, 5345–5352 (2019).
7. H. Lee, S. M. Dellatore, W. M. Miller, P. B. Messersmith, Mussel-inspired surface chemistry for multifunctional coatings. *Science* **318**, 426–430 (2007).
8. P. Yang, S. Zhang, X. Chen, X. Liu, Z. Wang, Y. Li, Recent developments in polydopamine fluorescent nanomaterials. *Mater. Horiz.* **7**, 746–761 (2020).
9. J. H. Ryu, P. B. Messersmith, H. Lee, Polydopamine surface chemistry: A decade of discovery. *ACS Appl. Mater. Interfaces* **10**, 7523–7540 (2018).
10. S. B. Darling, Perspective: Interfacial materials at the interface of energy and water. *J. Appl. Phys.* **124**, 030901 (2018).
11. Z. Wang, H. C. Yang, F. He, S. Peng, Y. Li, L. Shao, S. B. Darling, Mussel-inspired surface engineering for water-remediation materials. *Matter* **1**, 115–155 (2019).
12. M. d'Ischia, A. Napolitano, A. Pezzella, P. Meredith, M. J. Buehler, Melanin biopolymers: Tailoring chemical complexity for materials design. *Angew. Chem. Int. Ed.* **59**, 11196–11205 (2020).
13. H. A. Lee, Y. Ma, F. Zhou, S. Hong, H. Lee, Material-independent surface chemistry beyond polydopamine coating. *Acc. Chem. Res.* **52**, 704–713 (2019).
14. S. Hong, Y. S. Na, S. Choi, I. T. Song, W. Y. Kim, H. Lee, Non-covalent self-assembly and covalent polymerization co-contribute to polydopamine formation. *Adv. Funct. Mater.* **22**, 4711–4717 (2012).
15. P. Delparastan, K. G. Malollari, H. Lee, P. B. Messersmith, Direct evidence for the polymeric nature of polydopamine. *Angew. Chem. Int. Ed.* **131**, 1089–1094 (2019).
16. S. Hong, Y. Wang, S. Y. Park, H. Lee, Progressive fuzzy cation-π assembly of biological catecholamines. *Sci. Adv.* **4**, eaat7457 (2018).
17. T. G. Barclay, H. M. Hegab, S. R. Clarke, M. Ginic-Markovic, Versatile surface modification using polydopamine and related polycatecholamines: Chemistry, structure, and applications. *Adv. Mater. Interfaces* **4**, 1601192 (2017).
18. Y. Wang, W. Zhu, W. Du, X. Liu, X. Zhang, H. Dong, W. Hu, Cocrystals strategy towards materials for near-infrared photothermal conversion and imaging. *Angew. Chem. Int. Ed.* **57**, 3963–3967 (2018).
19. K. Bochenek, E. Gudowska-Nowak, Fundamental building blocks of eumelanins: Electronic properties of indolequinone-dimers. *Chem. Phys. Lett.* **373**, 532–538 (2003).
20. X. Guo, M. Zhang, J. Tan, S. Zhang, L. Huo, W. Hu, Y. Li, J. Hou, Influence of D/A ratio on photovoltaic performance of a highly efficient polymer solar cell system. *Adv. Mater.* **24**, 6536–6541 (2012).
21. W. Wu, Y. Liu, D. Zhu, π-Conjugated molecules with fused rings for organic field-effect transistors: Design, synthesis and applications. *Chem. Soc. Rev.* **39**, 1489–1502 (2010).
22. X. Wu, G. Y. Chen, G. Owens, D. Chu, H. Xu, Photothermal materials: A key platform enabling highly efficient water evaporation driven by solar energy. *Mater. Today Energy* **12**, 277–296 (2019).
23. J. Kaizer, J. Pap, G. Speier, Modeling antioxidant properties of polyphenols by the TEMPO-initiated reaction of 3,5-di-*tert*-butylcatechol with dioxygen. *Food Chem.* **93**, 425–430 (2005).
24. Y. I. Avila-Vega, C. C. Leyva-Porras, M. Mireles, M. Quevedo-López, J. Macossay, J. Bonilla-Cruz, Nitroxide-functionalized graphene oxide from graphite oxide. *Carbon* **63**, 376–389 (2013).
25. K. Ai, Y. Liu, C. Ruan, L. Lu, G. Lu, Sp2 C-dominant N-doped carbon sub-micrometer spheres with a tunable size: A versatile platform for highly efficient oxygen-reduction catalysts. *Adv. Mater.* **25**, 998–1003 (2013).
26. J. R. Pels, F. Kapteijn, J. A. Moulijn, Q. Zhu, K. M. Thomas, Evolution of nitrogen functionalities in carbonaceous materials during pyrolysis. *Carbon* **33**, 1641–1653 (1995).
27. M. Parracino, P. Pellacani, P. Colpo, G. Ceccone, A. Valsesia, F. Rossi, M. Manso Silvan, Biofouling properties of nitroxide-modified amorphous carbon surfaces. *ACS Biomater. Sci. Eng.* **2**, 1976–1982 (2016).
28. F. Bernsmann, V. Ball, F. Addiego, A. Ponche, M. Michel, J. J. D. A. Gracio, V. Toniazzo, D. Ruch, Dopamine–melanin film deposition depends on the used oxidant and buffer solution. *Langmuir* **27**, 2819–2825 (2011).
29. J. Zhou, Z. Lu, X. Zhu, X. Wang, Y. Liao, Z. Ma, F. Li, NIR photothermal therapy using polyaniline nanoparticles. *Biomaterials* **34**, 9584–9592 (2013).
30. P. K. Jain, X. Huang, I. H. El-Sayed, M. A. El-Sayed, Review of some interesting surface plasmon resonance-enhanced properties of noble metal nanoparticles and their applications to biosystems. *Plasmonics* **2**, 107–118 (2007).
31. Q. Song, Y. Jiao, Z. Wang, X. Zhang, Tuning the energy gap by supramolecular approaches: Towards near-infrared organic assemblies and materials. *Small* **12**, 24–31 (2016).
32. B. Lü, Y. Chen, P. Li, B. Wang, K. Müllen, M. Yin, Stable radical anions generated from a porous perylenediimide metal-organic framework for boosting near-infrared photothermal conversion. *Nat. Commun.* **10**, 767 (2019).
33. J. Wang, Y. Li, L. Deng, N. Wei, Y. Weng, S. Dong, D. Qi, J. Qiu, X. Chen, T. Wu, High-performance photothermal conversion of narrow-bandgap Ti_2O_3 nanoparticles. *Adv. Mater.* **29**, 1603730 (2017).
34. T. Okamoto, S. Kumagai, E. Fukuzaki, H. Ishii, G. Watanabe, N. Niitsu, T. Annaka, M. Yamagishi, Y. Tani, H. Sugiura, T. Watanabe, S. Watanabe, J. Takeya, Robust, high-performance n-type organic semiconductors. *Sci. Adv.* **6**, eaaz0632 (2020).
35. C. Liu, K. Wang, X. Gong, A. J. Heeger, Low bandgap semiconducting polymers for polymeric photovoltaics. *Chem. Soc. Rev.* **45**, 4825–4846 (2016).
36. K. Wu, W. E. Rodríguez-Córdoba, Y. Yang, T. Lian, Plasmon-induced hot electron transfer from the Au Tip to CdS rod in CdS-Au nanoheterostructures. *Nano Lett.* **13**, 5255–5263 (2013).
37. X. Wu, G. Y. Chen, W. Zhang, X. Liu, H. Xu, A plant-transpiration-process-inspired strategy for highly efficient solar evaporation. *Adv. Sustain. Syst.* **1**, 1700046 (2017).
38. Q. Jiang, H. Gholami Derami, D. Ghim, S. Cao, Y.-S. Jun, S. Singamaneni, Polydopamine-filled bacterial nanocellulose as a biodegradable interfacial photothermal evaporator for highly efficient solar steam generation. *J. Mater. Chem. A* **5**, 18397–18402 (2017).
39. X. Wu, Q. Jiang, D. Ghim, S. Singamaneni, Y.-S. Jun, Localized heating with a photothermal polydopamine coating facilitates a novel membrane distillation process. *J. Mater. Chem. A* **6**, 18799–18807 (2018).
40. Y. Zhang, X. Yin, B. Yu, X. Wang, Q. Guo, J. Yang, Recyclable polydopamine-functionalized sponge for high-efficiency clean water generation with dual-purpose solar evaporation and contaminant adsorption. *ACS Appl. Mater. Interfaces* **11**, 32559–32568 (2019).
41. S. Ma, C. P. Chiu, Y. Zhu, C. Y. Tang, H. Long, W. Qarony, X. Zhao, X. Zhang, W. H. Lo, Y. H. Tsang, Recycled waste black polyurethane sponges for solar vapor generation and distillation. *Appl. Energy* **206**, 63–69 (2017).
42. M. J. Frisch, G. W. Trucks, H. B. Schlegel, G. E. Scuseria, M. A. Robb, J. R. Cheeseman, G. Scalmani, V. Barone, G. A. Petersson, H. Nakatsuji, X. Li, M. Caricato, A. V. Marenich, J. Bloino, B. G. Janesko, R. Gomperts, B. Mennucci, H. P. Hratchian, J. V. Ortiz, A. F. Izmaylov, J. L. Sonnenberg, Williams, F. Ding, F. Lipparini, F. Egidi, J. Goings, B. Peng, A. Petrone, T. Henderson, D. Ranasinghe, V. G. Zakrzewski, J. Gao, N. Rega, G. Zheng, W. Liang, M. Hada, M. Ehara, K. Toyota, R. Fukuda, J. Hasegawa, M. Ishida, T. Nakajima, Y. Honda, O. Kitao, H. Nakai, T. Vreven, K. Throssell, J. A. Montgomery Jr., J. E. Peralta, F. Ogliaro, M. J. Bearpark, J. J. Heyd, E. N. Brothers, K. N. Kudin, V. N. Staroverov, T. A. Keith, R. Kobayashi, J. Normand, K. Raghavachari, A. P. Rendell, J. C. Burant, S. S. Iyengar, J. Tomasi, M. Cossi, J. M. Millam, M. Klene, C. Adamo, R. Cammi, J. W. Ochterski, R. L. Martin, K. Morokuma, O. Farkas, J. B. Foresman, D. J. Fox, Gaussian 16 Rev. B.01 (Wallingford, CT, 2016).

Acknowledgments

Funding: This work was supported by the National Natural Science Foundation of China (21975167 and 21774079) and the National Key R&D Program of China (2019YFA0904500).

Author contributions: Y.Z. carried out the synthetic work, conducted material characterizations, and made the devices. X.C. and P.Y. performed the photothermal experiments and discussion. G.L. and Y.Y. performed the transient absorption spectra testing. Z.G. finished the simulation work. Y.L. designed and supervised the study and wrote the manuscript. **Competing interests:** The authors declare that they have no competing interests. **Data and materials availability:** All data needed to evaluate the conclusions in the paper are present in the paper and/or the Supplementary Materials. Additional data related to this paper may be requested from the authors.

Submitted 26 February 2020
Accepted 21 July 2020
Published 4 September 2020
10.1126/sciadv.abb4696

Citation: Y. Zou, X. Chen, P. Yang, G. Liang, Y. Yang, Z. Gu, Y. Li, Regulating the absorption spectrum of polydopamine. *Sci. Adv.* **6**, eabb4696 (2020).